Molecular basis of neurodegeneration in a mouse model of *Polr3*-related disease

Robyn D. Moir[1,†]*, Emilio Merheb[1,†], Violeta Chitu[2], E. Richard Stanley[2] and Ian M. Willis[1,3]*

[1] Department of Biochemistry,

[2] Department of Developmental and Molecular Biology,

[3] Department of Systems and Computational Biology,

Albert Einstein College of Medicine, 1300 Morris Park Ave, Bronx NY 10461, USA

[†] R.D.M. and E.M. contributed equally to this work.

* Corresponding authors, Robyn D. Moir and Ian M. Willis

Email: robyn.moir@einsteinmed.edu and ian.willis@einsteinmed.edu

Abstract

Pathogenic variants in subunits of RNA polymerase (Pol) III cause a spectrum of neurodegenerative diseases including 4H leukodystrophy. Disease onset occurs from infancy to early adulthood and is associated with a variable range and severity of neurological and non-neurological features. The molecular basis of disease pathogenesis is unknown. We developed a postnatal whole-body mouse model expressing pathogenic *Polr3a* mutations to examine the molecular mechanisms by which reduced Pol III transcription results primarily in central nervous system phenotypes. *Polr3a* mutant mice exhibit behavioral deficits, cerebral pathology and exocrine pancreatic atrophy. Transcriptome and immunohistochemistry analyses of cerebra during disease progression show a reduction in most Pol III transcripts, induction of innate immune and integrated stress responses and cell type-specific gene expression changes reflecting neuron and oligodendrocyte loss and microglial activation. Earlier in the disease when integrated stress and innate immune responses are minimally induced, mature tRNA sequencing revealed a global reduction in tRNA levels and an altered tRNA profile but no changes in other Pol III transcripts. Thus, changes in the size and/or composition of the tRNA pool have a causal role in disease initiation. Our findings reveal different tissue- and brain region-specific sensitivities to a defect in Pol III transcription.

Introduction

Biallelic pathogenic mutations in multiple subunits of RNA polymerase (Pol) III are causally associated with a spectrum of neurodegenerative diseases (Lata et al. 2021; Watt et al. 2023). These *Polr3*-related disorders include a prevalent form of leukodystrophy with hypomyelination, hypodontia and hypogonadotropic hypogonadism (4H leukodystrophy) as distinguishing features along with cerebellar atrophy, myopia and short stature (Wolf et al. 2014). Patients with *Polr3*-related leukodystrophy typically present in early childhood with motor deficits and developmental delay. The disease is inherited in an autosomal recessive manner, is progressive and exhibits wide ranging phenotypic severity from premature death during infancy to mild forms that have been diagnosed in adults (Watt et al. 2023). The neurologic and non-neurologic manifestations of *Polr3*-related disorders are variably penetrant. Notably, initial findings of hypomyelination, suggesting oligodendrocyte involvement, are not universal as some patients have normal or near normal myelination but distinct MRI and neuropathological changes that suggest a largely neuronal phenotype (Perrier et al. 2022). Other atypical forms of *Polr3*-related disease have also been reported (Lata et al. 2021; Watt et al. 2023). The bases for these different disease presentations are unclear. It is also unclear why mutations in Pol III, a ubiquitously-expressed, essential enzyme responsible for the synthesis of critical non-coding RNAs central to protein synthesis, pre-mRNA splicing, secretion and other processes, result in phenotypes primarily of the central nervous system.

Phenotypic variability in *Polr3*-related disease is likely to reflect differences in the abundance of Pol III, its residual activity and how these changes affect the Pol III transcriptome at sensitive periods during embryonic and postnatal development. These properties are difficult to assess given the structural complexity of the 17 subunit Pol III enzyme and the fact that most patients carry compound heterozygous mutations that are likely to differentially affect enzyme function (Wolf et al. 2014). Genetic modifiers of *Polr3*-related phenotypes are also likely given

the observed phenotypic variation between unrelated patients with the same *Polr3* mutation (Bernard et al. 2011; Perrier et al. 2020). Few studies have examined the effect of pathogenic *Polr3* mutations on the levels of Pol III-derived transcripts in mammalian cells. Collectively, experiments with patient-derived fibroblasts and CRISPR-Cas9 engineered cell lines show that precursor tRNA levels are generally lower but only one of four mature tRNAs tested in two different studies were reduced, suggesting that high tRNA stability can compensate for defects in synthesis (Dorboz et al. 2018; Choquet et al. 2019). 7SL RNA levels were uniformly lower in agreement with a separate analysis of Pol III-derived transcripts in patient blood (Azmanov et al. 2016). Other Pol III-transcribed RNAs (5S RNA) showed discordant results or, based on one report, U6, Y, RPPH1, RMRP and 7SK RNAs were unchanged (Choquet et al. 2019). The extent to which the preceding findings reflect altered RNA levels in the brain is unknown.

In previous work we showed that brain-specific expression of pathogenic *Polr3a* mutations (W671R/G672E) in the mouse Olig2 lineage resulted in impaired growth and developmental delay, deficits in cognitive, sensory, and fine sensorimotor function, and hypomyelination in multiple regions of the cerebrum and spinal cord (Merheb et al. 2021). We report here a new model of *Polr3*-related disease in which expression of a Pol III enzyme bearing the *Polr3a* mutation is broadly induced postnatally in adolescent mice. Overt pathology was noted only in the exocrine pancreas and cerebrum despite similarly efficient recombination in multiple tissues. Analysis of the Pol III and Pol II transcriptomes reveal a common decrease in pre-tRNA and mature tRNA populations, few if any changes among other Pol III transcripts across multiple tissues, and activation of the integrated stress response in cerebra but not in other surveyed tissues. The molecular and cellular changes that underlie cerebral neurodegeneration in *Polr3a* mutant mice, which include induction of an innate immune response and activation of microglia, indicate different brain region-specific sensitivities to defective Pol III activity.

Results

A postnatal whole-body *Polr3a* mutant mouse

Patients with *Polr3*-related leukodystrophy express mutant forms of Pol III in all their cells. We sought to generate mice with a similarly broad cellular distribution of a Pol III enzyme bearing the *Polr3a* W671R/G672E mutation. To circumvent the embryonic lethality of the mutation, we employed a ubiquitously-expressed tamoxifen-inducible CAGGCre-ER^{TM} transgene to knockin the *Polr3a* mutant allele postnatally in diverse tissues (Hayashi and McMahon 2002). Five tamoxifen injections were administered every other day starting at postnatal day 28 (P28, Fig. 1A,B). Recombination frequencies determined by flow cytometry or fluorescence microscopy using a dual tdTomato-EGFP reporter were ~60% in liver, ~70% in cerebrum, ~80% in cerebellum and kidney and ~90% in heart (Supplementary Fig. S1). Tamoxifen-induced knockin mice (denoted as Polr3a-tamKI mice) have significantly lower body weights than tamoxifen-injected WT controls. Body weight differences appear in both sexes at P34 and become progressively larger as Polr3a-tamKI mice lose weight while the control mice gain weight over time (Fig. 1C). These differences are due in part to the smaller body size of Polr3a-tamKI mice post-injection (Fig. 1D), suggesting a growth defect. Notably, a growth defect was reported previously for Polr3a-Olig2KI mice (formerly Polr3a-cKI mice, Merheb et al. 2021), consistent with the reduced stature of many patients with Pol III-related leukodystrophy (Watt et al. 2023). However, in contrast to the current model, Polr3a-Olig2KI mice gain weight, albeit more slowly than controls, from adolescence to adulthood despite their smaller size (Merheb et al. 2021). Thus, the loss of body weight in Polr3a-tamKI mice demonstrates a more severe failure to thrive phenotype, in line with the widespread expression of the *Polr3a* mutation.

Impaired myelination and exocrine pancreatic atrophy

We conducted a broad histopathological analysis of the effect of the *Polr3a* mutation in adolescent (P42) and adult (P90) mice. Gross morphology was assessed by Hematoxylin and Eosin (H&E) staining and in the CNS, myelin and neurons were examined using Luxol Fast Blue (LFB) and Nissl, respectively. LFB staining of coronal sections of the cerebrum revealed impaired myelin deposition in Polr3a-tamKI cortex, hippocampus and thalamus with qualitatively greater differences in the cortex at P90 (Fig. 1E). In contrast, LFB- and Nissl-stained sagittal sections of the cerebellum showed no differences in myelin or granular layer neurons, respectively, and no difference in Purkinje cell density (Supplemental Fig. S2A,B). The absence of a myelination defect in the cerebellum was previously noted in Polr3a-Olig2KI mice (Merheb et al. 2021). Non-CNS tissues (>20 examined) were histologically normal except for the pancreas. Polr3a-tamKI mice exhibit pronounced and severe exocrine pancreatic atrophy at P42 and P90, respectively (Fig. 1F). This condition is characterized by insufficient production of digestive enzymes (Kleeff et al. 2017) and correlates with the lower body weight of Polr3a-tamKI mice, the marked reduction in subcutaneous and visceral adipose tissue at P90, and the poor health of the mice at this age. In contrast to the paucity of body fat at P90, echoMRI measurements at P42 showed that body fat as a percentage of total body weight was comparable to WT (Supplemental Fig. S2C). To assess whether the exocrine pancreatic defect might extend to the endocrine pancreas, glucose homeostasis was examined in adolescent mice. Blood glucose concentrations increased upon feeding, as expected, and were not significantly different between Polr3a-tamKI and WT mice in either the fasted or the refed state (Supplemental Fig. S2D). Similarly, a glucose tolerance test showed comparable responses (Supplemental Fig. S2E). These data suggest that endocrine pancreatic functions controlling glucose homeostasis are not significantly impaired at P42 by the *Polr3a* mutation.

Polr3a-tamKI mice exhibit multiple behavioral changes

A behavioral spectrometer with video tracking and pattern-recognition software was used to quantify ~20 home cage-like behaviors in a longitudinal study of behavior. Testing began at P42 and was continued at weekly intervals (Fig. 1B). No differences were observed in anxiety-like behavior, which was assessed using metrics that measure the natural tendency of mice to avoid open spaces (Supplemental Figs. S3A-C). However, overall locomotor activity was decreased in Polr3a-tamKI mice as indicated by the reduced track length at P42, P49, P56 and P63 (Fig. 2A). Polr3a-tamKI mice also spent less time running and more time standing still at all time points compared to WT mice, consistent with a locomotor deficit (Fig. 2B,C). Risk assessment was measured by orientation behavior according to three discrete metrics that can be summed to provide an overall evaluation of this behavior (Brodkin et al. 2014). Individual orientation behaviors were significantly lower in Polr3a-tamKI mice at all time points compared to WT mice, except for Orient-shuffle at P42 where there was a trend towards lower performance in the knockin mice (Supplemental Fig. S3D-F). The sum of these behaviors shows that Polr3a-tamKI mice spend less time assessing risk at all time points (Fig. 2D). Exploratory behavior was investigated via three rearing motions performed when the mice are standing on their hind legs. Polr3a-tamKI mice spent less time performing these motions at most timepoints and a tendency towards diminished performance at other times (Supplemental Fig. S3G-I). When all three rearing metrics were combined, Polr3a-tamKI mice showed lower levels of exploration compared to WT mice at all timepoints although the data did not reach significance at P49 (Fig. 2E). Grooming behavior was evaluated by measuring the time each animal spent attending to a specific region of their body (Fig. 2F; Supplemental Fig. S3J,K). The Polr3a-tamKI mice spent less time grooming their legs and back compared to WT mice starting at P49 and progressing to P63. Head grooming was also reduced at P63. In summary, the findings reveal behavioral phenotypes in Polr3a-tamKI mice at the earliest time point in the study, two weeks after introduction of the mutation, consistent with neurobehavioral deficits (Brodkin et al. 2014). As

none of the affected behaviors were apparent in Polr3a-Olig2KI mice (Merheb et al. 2021), the data further demonstrate that the mutation has a more severe impact on animal behavior when its expression is induced postnatally in many cell types than when it is induced during embryonic development only in the Olig2 lineage.

A reduction in Pol III transcripts in the cerebra of adult Polr3a-tamKI mice is accompanied by induction of innate immune and integrated stress responses

To investigate the molecular changes to Pol III transcript levels caused by the *Polr3a* mutation and the potential effect on the Pol II transcriptome, we initially focused on the cerebra of adult mice at P75. Precursor tRNA levels reflect Pol III transcription activity since these nascent RNAs are rapidly processed into mature sized tRNA by the removal of 5' leader, 3' trailer and, in some instances, intronic sequences (Berg and Brandl 2021). The levels of four precursor tRNAs, determined either by northern blotting for intron sequences or by RT-qPCR with precursor-specific primers, were reduced ~three-fold in Polr3a-tamKI cerebra (Fig. 3A-C). Mature tRNAs and other Pol III transcripts have relatively long half-lives and thus their levels reflect steady state abundance rather than synthesis (Nwagwu and Nana 1980). Nonetheless, northern blotting of four mature tRNAs showed that all were lower in Polr3a-tamKI cerebra with two of them reduced to ~60% of the WT (Fig. 3A,B).

Despite the defect in precursor tRNA synthesis and the reduction in mature tRNAs, the Pol III transcriptome was not universally affected (Fig. 3A-C). Transcripts from genes with a tRNA-like Type II promoter (e.g. 7SL, BC1 and vault RNA genes) showed a decrease in abundance to between 45% and 60% of the WT level (Fig. 3C). Transcripts from genes with a Type III promoter (e.g. U6, RMRP, RppH1 and 7SK genes), were variably decreased: RppH1 and 7SK RNAs were decreased to 70% and 56%, respectively, while U6, U6atac and RMRP

RNAs were unaffected. The level of 5S rRNA, the only RNA produced using a Type I promoter, was elevated (Fig. 3C).

Mouse models of neurodegeneration with underlying defects in the translation machinery induce an adaptive response to cellular stress known as the integrated stress response (ISR) (Ishimura et al. 2016; Abbink et al. 2019; Terrey et al. 2020; Spaulding et al. 2021). Canonical activation of the ISR is initiated by stress-activated protein kinases which phosphorylate eIF2α to globally attenuate bulk mRNA translation initiation, increase translation of uORF-containing mRNAs including transcription factors such as ATF4 and induce a stress response transcription program (Costa-Mattioli and Walter 2020). We measured the expression of 10 ATF4-regulated ISR target genes to evaluate whether the ISR had been activated in Polr3a-tamKI cerebra. A two to six-fold upregulation was measured for seven of these genes, two others were induced at lower levels and one was unaffected (Fig. 3D). These results point to altered translation in Polr3a-tamKI cerebra.

Bulk RNAseq was used to broadly profile the transcriptional changes in Polr3a-tamKI cerebra at P75. Differentially expressed (DE) genes (p adj. <0.05, log2FoldChange >|0.58|) were biased towards upregulation; 83% of DE genes were increased in the *Polr3a* mutant (Fig. 3E; Supplemental Table S1). We compared our DE genes with a list of 774 ISR genes that show ATF4-dependent induction following tunicamycin treatment of mouse embryo fibroblasts (Torrence et al. 2021) and found 192 genes upregulated in Polr3a-tamKI cerebra (Fig. 3E, annotated in green, Supplemental Fig. S4A; Supplemental Table S1). Among these were key ISR regulators, such as uORF-containing transcription factors (ATF3, ATF5 and CHOP, aka Ddit3), pro-apoptotic targets of CHOP (Chac1 and Bbc3), and negative ISR regulators (PPP1r15a, aka GADD34 and TRIB3) that function to antagonize the response (Fig. 3E). Interestingly, expression of the transcription factor ATF6 and its canonical ERAD targets (Pdia4, Pdia6, EDEM1, GRP78 aka Hspa5, GRP94 aka Hsp90b1, XBP1 and calnexin) were not

affected suggesting that ISR induction in the *Polr3a* mutant does not involve an ER stress-mediated Unfolded Protein Response (UPR, Supplemental Table S1)(Hillary and FitzGerald 2018). This was confirmed by showing that the relative levels of inactive unspliced and active spliced forms of XBP1, a critical transcription factor for the UPR, were unchanged (Supplemental Fig. S4B).

Metascape pathway enrichment of upregulated DE genes identified activation of the immune system and related processes as major functional categories (Fig. 3F; Supplemental Table S1). These data point to activation of microglia (see below) and the upregulation of signaling pathways that promote inflammation and cell death by multiple mechanisms (Butovsky and Weiner 2018). For example, pyroptosis is indicated by the upregulation of caspases 1 and 4, the inflammasome sensor NLRP3 and its adapter protein, PYCARD, interleukin-1β and the plasma membrane pore-forming protein, Gasdermin D, among others (Supplemental Table S1). The most enriched functional categories among genes down-regulated in Polr3a-tamKI cerebra were cholesterol biosynthesis and electron transport (Supplemental Table S1). All mitochondrially-encoded transcripts were also down-regulated in the *Polr3a* mutant (Fig. 3E, annotated in blue). In contrast, nuclear-encoded mitochondrial genes were mostly unaffected although 24 were found in the upregulated gene set (Supplemental Table S1; Supplemental Fig. S4C). These observations suggested a loss of mitochondrial DNA. Indeed, qPCR analysis showed that the ratio of two mitochondrial genes (16S rRNA and ND1) to a nuclear gene (HK2) was substantially reduced in Polr3a-tamKI cerebra (Supplemental Fig. S4D). Thus, the loss of mitochondrial genomes underlies the reduction in mitochondrially-encoded RNA detected by RNAseq. *Hmgcr* and *Sqle* were among numerous sterol biosynthetic genes down-regulated in Polr3a-tamKI cerebra (Supplemental Fig. S4E; Supplemental Table S1). These enzymes function in rate-limiting steps in *de novo* cholesterol synthesis, suggesting dysfunctional cholesterol production. Cholesterol synthesis in the brain occurs predominantly in astrocytes

and oligodendrocytes, accounts for almost one quarter of total body cholesterol and cannot be compensated by the periphery since cholesterol uptake is blocked by the blood-brain barrier (Saher and Stumpf 2015). Astrocytes synthesize cholesterol for export to neurons while oligodendrocytes (OLs) synthesize 70-80% of brain cholesterol that resides in myelin (Barber and Raben 2019; Li et al. 2022). Impairment of cholesterol biosynthesis in either cell type can result in cognitive and behavioral phenotypes (Li et al. 2022) and thus may contribute to the behavioral defects noted in Polr3a-tamKI mice.

Changes in cell-type specific gene expression reflect the loss of neurons and oligodendrocytes and activation of microglia

We queried the Polr3a-tamKI DE genes against consensus sets of mouse brain cell type gene expression signatures for OLs, neurons, astrocytes, microglia and endothelial cells (McKenzie et al. 2018). Twenty-one percent of Polr3a-tamKI DE genes (p-adj <0.05) could be assigned to one of these five cell types with microglia and neurons constituting the bulk of the cell type-specific genes (Supplemental Table S2). OL and neuronal gene expression was predominantly down-regulated suggesting a reduction in these cell populations while microglia were predominantly elevated (Fig. 4A-C; Supplemental Table S2). Immunohistochemistry confirmed that these changes in cell type gene expression signatures correlated with changes in cell-specific protein markers (Fig. 4D-H). Myelination in the mouse begins at birth and is largely complete by weaning although it continues with decreasing frequency through adulthood (Hammelrath et al. 2016; Nishiyama et al. 2021). Thus, under our treatment regimen, substantial myelination has occurred by P28 when the *Polr3a* mutation is introduced. This, together with the long half-life of myelin (Barnes-Velez et al. 2023) contributes to a high background level of myelin. Accordingly, the mean fluorescence intensity of myelin basic protein (MBP) staining in the corpus callosum of adult Polr3a-tamKI mice was not significantly

diminished relative to WT. However, the density of MBP staining was reduced as was the number of OLs staining positive with the CC1 antibody (Fig. 4D,E). In the cerebral cortex, the mean fluorescence intensity of NeuN staining and the number of NeuN positive neuronal nuclei was lower in Polr3a-tamKI mice (Fig. 4F) consistent with the decrease in neuron-specific gene expression. Additionally, we observed reactive microglia in Polr3a-tamKI cerebra, as evidenced by the increased cell density and altered morphology (enlarged cell bodies and shorter, thicker processes) of Iba1-stained cells in the cortex and particularly in the striatum (Fig. 4G,H). Together, these data indicate that behavioral deficits, induction of the ISR, loss of mitochondrial genomes, an elevated immune response and neurodegeneration are causally linked to the loss of Pol III transcription in Polr3a-tamKI cerebra.

To assess whether the changes observed in Pol III and Pol II transcripts in P75 cerebra occurred in other tissues, we examined cerebellum, heart, kidney and liver from the same animals. The levels of three precursor tRNAs in the cerebellum, heart, kidney were reduced ~three-fold, comparable to the changes seen in cerebra (Supplemental Fig. S5A). However, in the liver, where the efficiency of CAGGCre-ER^{TM} recombination is lower (Supplemental Fig. S1C; Hayashi and McMahon 2002), only one of the three precursor tRNAs was reduced (Supplemental Fig. S5A). The levels of two mature tRNAs were variably affected, being unchanged in liver and cerebella, trending lower in heart and reduced in kidney to ~70% of WT (Supplemental Fig. S5A). Among other Pol III transcripts, tissues other than cerebra showed few changes: 7SL and RMRP RNA levels were reduced in cerebella but otherwise no reductions were detected (Supplemental Fig. S5B). Similarly, there was little indication of an ISR response in the tested tissues other than cerebra (Supplemental Fig. S5C). These data imply that the diminished activity of Pol III in these tissues is above the threshold necessary for ISR induction.

A reduction in Pol III transcription and mature tRNA levels precedes induction of innate immune and integrated stress responses

To separate causal changes in Pol III activity from secondary stress responses that could down-regulate Pol III transcription, we profiled the Pol II and Pol III transcriptomes of WT and Polr3a-tamKI cerebra at P42, two weeks after induction of recombination. Similar to the P75 time point, Polr3a-tamKI pre-tRNA levels were reduced ~three-fold and three out of four mature tRNAs were reduced to ~60% of the WT level (compare Fig. 5A-C with Fig. 3A-C). No Pol III transcripts other than tRNAs were decreased at P42 (Fig. 5C). Thus, decreased production of precursor and mature tRNA is the earliest detectable Pol III defect in Polr3a-tamKI cerebra.

Analysis of the ATF4-regulated ISR gene panel revealed that fewer genes were induced in Polr3a-tamKI cerebra at P42 and the response was less robust than at P75 (compare Supplemental Fig. S6A and Fig. 3D). Sesn2, Mthfd2, Chac1, Ald1l2 and Asns were up-regulated two-fold or less indicating partial activation of the ISR. Bulk RNAseq showed fewer significant DE genes at P42 (181 genes) with 68% up-regulated and minimal overlap with the P75 DE gene set (Fig. 5D; Supplemental Fig. S6B; Supplemental Table S3). Although no GO terms were enriched, the P42 DE gene set contained a small number of ISR genes (20 genes), the majority of which are ATF4-regulated and showed increased expression (Supplemental Fig. S6B; Supplemental Table S3). Similarly, a small number of up-regulated genes were associated with the immune response GO bioprocess (21 genes at P42 versus 582 genes at P75, Supplemental Table S3). Expression of mitochondrially-encoded genes was unaffected at P42, as was mitochondrial genome content (Supplemental Fig. S6C; Supplemental Table S3). Together these data indicate a progression of stress and immune response programs with time in Polr3a-tamKI cerebra.

The *Polr3a* mutation reduces total cytoplasmic tRNA levels and alters the tRNA profile

The effect of the *Polr3a* mutation on the tRNAome in P42 cerebra was assessed by QuantM-tRNA-seq (Pinkard et al. 2020). This method exploits the conserved 3'-CCA end of mature tRNAs using a splint-ligation approach to prepare DNA libraries for sequencing. Prior to sample workup, a synthetic tRNA spike-in based on *E. coli* $tRNA^{Gln}$ was added for normalization of tRNA reads to total input RNA. Since mitochondrially-encoded mRNAs and mitochondrial DNA content were comparable between WT and Polr3a-tamKI cerebra at P42 (Supplemental Fig. S6C; Supplemental Table S3), mitochondrially-encoded tRNAs were also used for normalization. Total nuclear-encoded tRNA reads normalized with either or both standards were similar and significantly lower in Polr3a-tamKI cerebra suggesting an ~25% reduction in total tRNA abundance (Fig. 6A; Supplemental Fig. S6D,E). Differential expression (DE) analysis indicated that the majority of tRNA isodecoders (i.e. tRNAs that share the same anticodon but have different body sequences) were significantly lower in the *Polr3a* mutant (58%, 108/187 tRNAs with p-adj < 0.05, Supplemental Table S5). DE was observed across the entire read depth which spans 5 orders of magnitude and included tRNAs whose sequences could be uniquely mapped as well as redundantly-encoded tRNAs (Fig. 6B). Compared to most elongator tRNAs, the three $tRNAi^{Met}$ isodecoders were less dramatically affected, reduced to 86-88% of the WT level. The level of tRNAArg-TCT-4-1 (aka *Tr20*), an abundant neuron-enriched tRNA that is mutated in the C57BL/6J background and causes synthetic phenotypes when combined with ribosome rescue factor mutants (Ishimura et al. 2014; Terrey et al. 2020), was unchanged in the *Polr3a* mutant. Thus, the cerebral phenotypes of Polr3a-tamKI mice are unlikely to result from synthetic effects of the tRNAArg-TCT-4-1 and *Polr3a* mutations.

Grouping tRNA isodecoders into their isoacceptor families illustrates that most members of each family were reduced in the *Polr3a* mutant (Fig. 6C). Indeed, when tRNA read counts were combined into their respective decoder (i.e. anticodon) groups, all decoders were reduced in the *Polr3a* mutant, and for 30 decoders (60%), the reductions were significant (Fig. 6F;

Supplemental Table S5). To assess how these changes affect the composition of the tRNA population (i.e. the tRNA profile), each decoder was plotted as a percentage of the total tRNA population for the *Polr3a* mutant versus WT (Fig. 6E). This revealed changes in the relative proportions of some tRNAs. For example, $tRNA^{Val}$(AAC) and $tRNA^{Tyr}$(GTA) were proportionally less abundant than $tRNA^{His}$(GTG), and seven other tRNAs, respectively. These changes coupled with the overall decrease in tRNA abundance have the potential to change the kinetics of tRNA binding to the ribosome (decoding speed) as well as the kinetic competition with near-cognate tRNAs for ribosome binding. The most severely affected decoders were $tRNA^{Val}$(AAC) (to 48% of the WT level), $tRNA^{Tyr}$(GTA) (to 50%), $tRNA^{Sup}$(TCA) (to 53%), $tRNA^{Ser}$(AGA) (to 63%) and $tRNA^{Gln}$(CTG) (to 64%). In mouse, $tRNA^{Ser}$(AGA) and $tRNA^{Val}$(AAC) decode 41% and 42% of their respective codons (accounting for 3rd base wobble), $tRNA^{Gln}$(CTG) decodes 75% of glutamine codons and $tRNA^{Tyr}$(GTA) decodes 100% of tyrosine codons. These findings suggest that the decrease in tRNA decoders is likely to negatively affect the tRNA decoding potential at the earliest stage of disease pathogenesis.

All tRNA isodecoder families are reduced in Polr3a-tamKI cerebellum but few decoders are affected

An initial analysis of the Pol III transcriptome in Polr3a-tamKI cerebella at P42 revealed comparable findings to the cerebra with decreases in several precursor and mature tRNAs and no effects on other Pol III transcripts (compare Supplemental Fig. S7A,B with Fig. 5B,C). QuantM-tRNA-seq indicated that total tRNA abundance was reduced in cerebella by ~23% in the *Polr3a* mutant (Supplemental Fig. S7D), similar to cerebra, and the expression of tRNA isodecoders was broadly decreased (Supplemental Fig. S7E,F). However, a comparative DE analysis showed that fewer tRNAs (30 versus 108) and fewer tRNA decoders (11 versus 30) achieved statistical significance in Polr3a-tamKI cerebella compared to cerebra (Fig. 6G,H;

Supplemental Table S6) and the distribution of fold change values spanned a narrower range and was shifted towards smaller differences relative to WT (Fig. 6D). In addition, the tRNA profile was minimally altered in cerebella (Supplemental Fig. S7G). These differential effects on the tRNA population in cerebella versus cerebra are consistent with bulk RNA-seq data from cerebella which showed few significant DE genes (13 genes, p-adj <0.05, log2Fold Change >|0.58|, Supplemental Table S4) and limited overlap with cerebral DE genes (Supplemental Fig. S7C). The minimal effect of the *Polr3a* mutation on the Pol II transcriptome of cerebella at P42 and the absence of ISR induction at P75 suggests that any reduction in tRNA decoding potential is insufficient to cause significant pathology in this tissue.

Discussion

Patients with *Polr3*-related disease express *Polr3* mutations in all cells during development and throughout postnatal life yet exhibit predominantly CNS phenotypes. To gain insight into this neural sensitivity, we introduced a pathogenic *Polr3a* mutation into mice using a ubiquitously-expressed tamoxifen-inducible Cre recombinase and examined the effects of reduced Pol III transcription in various tissues in a largely post-developmental state. The paucity of gross phenotypes identified by histopathology across many *Polr3a* mutant tissues reflects that cell-specific requirements for a minimum threshold of Pol III transcription have mostly been met. At the molecular level, our analysis of heart, kidney, cerebella and cerebra showed that Pol III transcription, as reported by pre-tRNA levels, was substantially reduced at P75, six weeks after induction of the mutation. These changes were paralleled by smaller decreases in mature tRNAs (Supplemental Fig. S5A) suggesting that tRNA half-lives are either much longer than expected in WT mice (Nwagwu and Nana 1980) and/or that tRNA turnover is decreased in the *Polr3a* mutant. Surprisingly, the levels of non-tRNA Pol III transcripts were not decreased in heart or kidney and only 7SL and RMRP RNAs were lower in cerebella at P75. In contrast,

reductions among non-tRNA transcripts were widespread in cerebra at the same age although two RNAs remained unaffected (Supplemental Fig. S5B). Given the levels of recombination in these tissues (which were higher in cerebella, kidney and heart than in cerebra, Supplemental Fig. S1C), the results point to a particularly high sensitivity of cerebra to the *Polr3a* mutation and a remarkable insensitivity of many non-tRNA transcripts in cerebella, kidney and heart to the reduction in Pol III activity. This insensitivity of non-tRNA transcripts may result from tissue-specific differences in the recruitment of the mutant Pol III to its genes, differences in the stability or nuclease accessibility of the RNA in specific ribonucleoprotein complexes, the ability of some Pol III promoters to be transcribed by RNA polymerase II (James Faresse et al. 2012; Dergai et al. 2018; Gao et al. 2018) or other effects that remain to be defined.

The higher sensitivity of cerebra versus cerebella, heart and kidney to the *Polr3a* mutation was apparent at both P42 and P75. In cerebella, only 13 DE genes were identified at P42 whereas in cerebra the number of DE genes was more than an order of magnitude higher and included a nascent ATF4-dependent ISR that was absent in cerebella at this age. Moreover, while the induction of ISR genes in cerebra increased at P75, there was no appreciable ISR induction in cerebella, heart and kidney. Together, these data suggest different thresholds of sensitivity to defects in Pol III transcription in different tissues and/or cell populations. Indeed, within the cerebra, the more robust activation of microglia in the striatum versus the cortex suggests significant differences in sensitivity to the *Polr3a* mutation between these regions. Thus, different thresholds of Pol III activity may be needed to support the functions of these regions, e.g. the continuing maturation of cortical thickness and myelination that occurs from P28 into adulthood (Hammelrath et al. 2016; Nishiyama et al. 2021) versus the functions other cells such as medium spiny neurons that comprise ~95% of the neurons in the striatum (Tepper and Bolam 2004).

In contrast to the cerebra, the apparent insensitivity of the cerebella to the *Polr3a* mutation may reflect that neurogenesis and synapse formation is largely complete by P21, before introduction of the mutation (Zeiss 2021). However, it remains possible that more subtle phenotypes such as dendritic pruning, which continues in the cerebellum through two months of age, may be affected (Leto et al. 2016). Of note, our developmental oligodendrocyte lineage model (Polr3a-Olig2KI mice), which showed reduced growth and neurological deficits along with hypomyelination in the cerebra and spinal cord (Merheb et al. 2021), also did not show cerebellar phenotypes. Together, these observations suggest that oligodendrocyte lineage cells in the cerebellum have a different threshold for minimal Pol III activity through development and maturation than in other regions of the brain.

The sensitivity of the mouse exocrine pancreas to the *Polr3a* mutation was unexpected given the absence of reports on acinar dysfunction associated with *Polr3*-related disease but is consistent with the knowledge that a *Polr3b* mutation disrupts development of the exocrine pancreas and intestine in zebrafish (Yee et al. 2007). Thus, our finding may inform undiagnosed digestive issues in the patient population. The unique codon usage of mouse and human pancreatic acinar cells, which differs from most other cell types and is skewed by the codon composition of highly expressed secreted proteins may underlie this phenotype (Gao et al. 2022). Alternatively, the *Polr3a* pancreatic phenotype may reflect unique differences in the development of rodent versus human pancreata: The increase in the size of mouse pancreas from birth to adulthood results largely from an increase (~19-fold) in the volume of acinar cells (Anzi et al. 2018). This hypertrophy of murine acinar cells is attributed to their higher biosynthetic rate and tetraploid genome content. In contrast, postnatal growth of human pancreas involves an increase in cell number, with acinar cells maintaining a constant volume (Anzi et al. 2018).

The reduction in the cerebral tRNA population at P42 coincides with behavioral deficits and precedes substantial alterations in the Pol II transcriptome, including induction of an innate immune response (IR) and an ISR, and indicators of neurodegeneration (activation of cell death pathways and loss of mitochondrial DNA), suggesting a causal role for the lower tRNA abundance and/or altered tRNA profile in disease progression. Whether the decrease in the abundance of other Pol III transcripts in the cerebrum at later times contributes to disease progression is an open question. These changes may represent secondary effects of IR/ISR signaling or cell death stressors and may be occurring in cells that have already committed to a pathway of programmed cell death.

Recent studies have shown that decreased levels of a single cytoplasmic tRNA isoacceptor or deletion/mutation of a single nuclear-encoded tRNA gene is sufficient to alter translation and cause neuronal dysfunction: Dominant mutations in the glycyl-tRNA synthetase gene associated with Charcot-Marie-Tooth disease CMT2D, cause sequestration of $tRNA^{Gly}$, neuropathy, impair neuronal translation and induce the ISR (Spaulding et al. 2021; Zuko et al. 2021). Mutation or deletion of the tRNAArg-TCT-4-1 isodecoder expressed in neurons, reduced the total $tRNA^{Arg}_{UCU}$ pool, caused ribosome pausing at AGA codons, ISR induction, defects in neuronal function and sensitization to loss of ribosome quality control proteins (Ishimura et al. 2014; Kapur et al. 2020; Terrey et al. 2020). Global deletion of the tRNAPhe1-1 isoacceptor is sufficient to cause transcription and proteomic changes, neurological deficits, increased ribosome stalling, and altered protein expression (Hughes et al. 2023). In the cerebra of Polr3a-tamKI mice, the induction of an ATF4-dependent ISR at P42 and its enhancement at P75 is a clear indicator that translation kinetics have been impacted by the global decrease in tRNA abundance, which extends across most decoders and changes the tRNA profile. Accordingly, the *Polr3a* mutation is predicted to compromise translation efficiency and change the frequency and sites of ribosome pausing and/or stalling. These events can trigger ISR induction via protein

misfolding or unresolved ribosome collisions (Costa-Mattioli and Walter 2020; Park et al. 2021). We propose that in the context of *Polr3*-related disease, chronic ISR activation ultimately fails to restore cellular homeostasis, and thus leads to neurodegeneration through amplification of the IR and activation of cell death pathways (Costa-Mattioli and Walter 2020).

Materials and Methods

Mouse husbandry

All experiments involving mice were performed using protocols approved by the Institutional Animal Care and Use Committee of the Albert Einstein College of Medicine (AECOM). Mice were housed in a barrier facility at 22°C on a 12-hour light/dark cycle with constant access to food (PicoLab® Mouse Diet 20) and water. C57BL/6J-*Polr3a*^{tm1Iwil} mice were described previously (Merheb et al. 2021) and were bred to B6.Cg-Tg(CAG-cre/Esr1*5Amc/J) mice (CAGGCre-ER^{TM}, #004682) and to B6.129(Cg)-Gt(ROSA)26Sor$^{tm4(ACTB\text{-}tdTomato,\text{-}EGFP)Luo}$/J mice (tdTomato-EGFP, #007676*).* Whole-body inducible *Polr3a* mutant mice and Cre-minus WT controls were obtained by breeding male mice heterozygous for both the floxed *Polr3a* allele and Cre recombinase to female mice homozygous for the floxed *Polr3a* allele. The breeding of mice to assess recombination used females homozygous for the tdTomato-EGFP reporter. Experimental animals (knockin mutants and WT controls) were treated with tamoxifen (6 mg/40 g body weight, five injections i.p.) every other day starting at P28. Unless otherwise indicated, all experiments were performed with male and female mice and the data were pooled for analysis.

Recombination efficiency

Single cell suspensions of dissected cerebrum and cerebellum were prepared using an adult brain dissociation kit (Miltenyi). Flow analysis was performed on a LSRII-U flow cytometer (BD

Biosciences) with single color controls to establish gating prior to sample analysis (Merheb et al. 2021). For liver, heart and kidney, fixed, sectioned tissue was mounted with ProLong diamond antifade with DAPI (Invitrogen) and imaged using a 3D Histech p250 high-capacity slide scanner. Manual cell counts were performed in ImageJ (five sections/tissue, >150 cells/section).

Purkinje Cell Counts

Images of Nissl-stained sagittal sections of cerebellum were viewed using CaseViewer software for manual counting of Purkinje cells in lobes III, IV/V, VI/VII and VIII. The open polygon tool was used to measure the length of the Purkinje layer for calculating Purkinje cell density.

Histology

Necropsy and staining of tissues with H&E, LFB and Nissl was performed in the Histopathology and Comparative Pathology Facility at AECOM. Images were acquired using a 3D Histech p250 high-capacity slide scanner.

Mouse behavior

Behavioral studies were conducted using a Behavioral Spectrometer (BiObserve) equipped with video-tracking, infrared beams and a vibration-sensitive floor. Locomotor activity was tracked and stereotyped behaviors were measured algorithmically using Viewer Software (BiObserve)(Brodkin et al. 2014). Individual mice were placed in the behavioral spectrometer for a total time of nine minutes at weekly intervals starting at P42 and finishing at P63.

Immunohistochemistry

Mice at P63-P66 were transcardially perfused with 4% paraformaldehyde (PFA), brains were removed and postfixed overnight in 4% PFA at 4°C before storage in 25% sucrose. Brains were

embedded in OCT medium, cut into 10 μm thick matched sections and stored at -20°C. Sections were post-fixed in 4% PFA for 10 min. at room temperature and rinsed in PBS 3x 5 min before permeabilization and blocking in 1% Triton X-100, 10% goat serum, 10% BSA, PBS for 2 hours at room temperature prior to staining. Slides were incubated overnight at 4°C with primary antibodies, MBP (Abcam Cat# ab7349, RRID:AB_305869; 1:100), CC1 (Millipore Cat# OP80, RRID:AB_2057371; 1:20) or NeuN (Abcam Cat# ab104224, RRID:AB_10711040; 1:100) in 0.1% Triton X-100, 1% goat serum, 10% BSA, PBS and then washed with PBS 3x 5 min. Secondary antibodies (1:1000) were conjugated to Alexa-Fluor 488 (Invitrogen A28175), Alexa-Fluor 568 (Invitrogen A21144) or Alexa Fluor 633 (Invitrogen A21094). For Iba1 staining, antigen retrieval (0.025% Tween-20 in 10 mM citrate buffer pH 6.0) and non-specific blocking (10% donkey serum) was performed before incubation overnight with primary antibody (Wako Chemicals RRID:AB_839504; 1:250) and detection with IgG conjugated to Alexa 488 (Invitrogen A11008). After washing in PBS, slides were mounted with ProLong diamond antifade with DAPI (Invitrogen). Images were captured using a 3D Histech P250 High Capacity Slide Scanner and Z-stack images were acquired using a Leica SP8 inverted DMi8 confocal microscope (40X N.A.1.3).

Immunofluoresence and quantitation

LIF micrographs were analyzed using Volocity software. Composite images were generated and then split into individual channels. The threshold for the green, red and magenta channels was set uniformly across all sections according to signal intensity. Mean fluorescent intensity and area values were reported directly from Volocity software. CC1 stained cells were counted at the midline of the corpus callosum and NeuN stained cells were counted in the motor cortex. Colocalization of CC1 and MBP signals was interrogated in the merged image throughout the Z-

stack and confirmed in the individual split channels. Quantification of Iba1 straining was performed manually in areas covering ~1.3 mm^2 of the cortex and striatum.

Nucleic acid preparation for RNA and DNA analysis

Tissues (50 to 100 mg, freeze-clamped and flash frozen in liquid nitrogen) were homogenized into TRIzol Reagent. RNA was reprecipitated before quantification. DNA recovered using the TRIzol DNA isolation protocol was used in mitochondrial genome content assays (Quiros et al. 2017). Total RNA (2µg) was used for cDNA synthesis with SuperScript III (SSIII, Invitrogen). qPCR followed the Lightcycler 480 SYBR Green I Master mix product manual for 384 multiwell plates (Roche). All primers are listed in Supplemental Table S7. Each sample was run in triplicate with 4-6 biological replicates. $\Delta\Delta$Ct values were calculated using two reference genes (GAPDH, β-actin and/or γ-tubulin)(Taylor et al. 2019).

Northern blotting

Total RNA (5µg) was resolved by denaturing polyacrylamide electrophoresis before electrophoretic transfer to Nytran N or SPC membranes (Cytiva), and hybridization to [^{32}P]-end-labeled oligonucleotide probes at 37°C (Bonhoure et al. 2015). Transcripts detected by phosphorimaging were quantified using ImageQuant software, normalized to U3 snRNA, and expressed as a fraction of the mean WT value. Oligonucleotide probes are listed in Supplemental Table S7.

tRNA-sequencing and differential expression analysis

Total RNA was mixed with a synthetic spike-in tRNA based on *E. coli* tRNAGln (Supplemental Table S7). The spike-in tRNA was denatured and refolded (80°C 2 min with a 0.1°C/s ramp to 20°C in 0.5 mM EDTA), and then added to 2.5 µg of total RNA from P42 cerebra (0.375 ng

spike-in) or P42 cerebella (0.750 ng spike-in) prior to tRNA library preparation. The RNA mixture was deacylated (37°C for 45 minutes in 20 mM Tris-HCl pH 9.0, RNaseOUT (1 µg/µL, Invitrogen) and then 3'-end dephosphorylated and 5'-end phosphorylated using T4 polynucleotide kinase (NEB). tRNA library preparation used SuperScript™ IV following the QuantM-tRNA-seq protocol (Pinkard et al. 2020). Library multiplexing, sequencing (Illumina NextSeq500, single-end 150 bp reads) and mapping was performed by the Center for Epigenomics/Computational Genomics Core at AECOM. Library reads were trimmed and mapped, as specified previously (Pinkard et al. 2020), to a custom look-up table containing the high confidence set of nuclear-encoded cytosolic tRNAs (gtRNAdb grcm38/mm10), mitochondrially-encoded tRNAs (RNAcentral) and the spike-in tRNA sequence. tRNA reads > 10 were used for further analyses. Decoder families were created by summing reads for all tRNAs with the same anticodon sequence. tRNAseq raw read counts for tRNAs and tRNA decoder families were normalized to the mitochondrial tRNA and spike-in tRNA read counts using the estimateSizeFactors control gene function in DESeq2 (Love et al. 2014). Differential expression and significance were determined using the likelihood ratio test (LRT) in DESeq2. Data visualization and plotting was performed in Prism (v9, GraphPad).

RNAseq

Poly(A) selected mRNA libraries were generated from total RNA (RINs > 8.9, Agilent Bioanalyzer), sequenced (Illumina PE150) and processed by Novogene. Differential expression and significance was determined using DESeq2 in R studio for all read counts >10 using default settings and the Wald test. DE was defined as adjusted p-value < 0.05. Downstream data visualization and plotting were performed using pheatmap in R and Prism (v9, GraphPad).

Statistical analysis

Statistical analyses were performed using Prism (v9 GraphPad) or Excel. Two-tailed unpaired Student's t tests were used for experiments with two conditions. Behavioral testing used multiple unpaired t tests and one-way ANOVAs. In molecular analyses, all samples represent biological replicates (no samples were pooled). Significance was determined at $p < 0.05$. * $p < 0.05$, ** $p < 0.01$, *** $p < 0.001$. Data are presented as mean ± standard deviation (SD) or ± standard error (SEM) as indicated. RNA-seq and QuantM-tRNA-seq data are available on the Gene Expression Omnibus (GEO) under accession number GSE246162.

Competing Interest Statement

The authors declare no competing interests.

Acknowledgments

We thank Hillary Guzik for her help with confocal image acquisition and Volocity analysis, Dr. Robert A. Dubin for computational support in mapping tRNAseq reads and Jinghang Zhang, M.D. for support with flow cytometry. This work was supported by a National Institutes of Health grant R21-NS123730 (to IMW and RDM). Additional support was provided by the Rose F. Kennedy Intellectual and Developmental Disabilities Research Center (IDDRC), which is funded through a center grant from the Eunice Kennedy Shriver National Institute of Child Health & Human Development (NICHD U54-HD090260), by an Albert Einstein Cancer Center core support grant (P30-CA013330) and Analytical Imaging facility support grants (1S10OD026852 & 1S10OD023591).

Author Contributions

R.D.M., E.M. and I.M.W. conceived the study. R.D.M., E.M., V.C. and I.M.W. performed the research and analyzed the data. E.R.S. and I.M.W. supervised the research. R.D.M, E.M and

I.M.W wrote the manuscript with contributions from the other authors. All authors read and approved the final version of the manuscript.

References

Abbink TEM, Wisse LE, Jaku E, Thiecke MJ, Voltolini-Gonzalez D, Fritsen H, Bobeldijk S, Ter Braak TJ, Polder E, Postma NL et al. 2019. Vanishing white matter: deregulated integrated stress response as therapy target. *Ann Clin Transl Neurol* **6**: 1407-1422.

Anzi S, Stolovich-Rain M, Klochendler A, Fridlich O, Helman A, Paz-Sonnenfeld A, Avni-Magen N, Kaufman E, Ginzberg MB, Snider D et al. 2018. Postnatal Exocrine Pancreas Growth by Cellular Hypertrophy Correlates with a Shorter Lifespan in Mammals. *Dev Cell* **45**: 726-737.

Azmanov DN, Siira SJ, Chamova T, Kaprelyan A, Guergueltcheva V, Shearwood AJ, Liu G, Morar B, Rackham O, Bynevelt M et al. 2016. Transcriptome-wide effects of a POLR3A gene mutation in patients with an unusual phenotype of striatal involvement. *Hum Mol Genet* **25**: 4302-4314.

Barber CN, Raben DM. 2019. Lipid Metabolism Crosstalk in the Brain: Glia and Neurons. *Front Cell Neurosci* **13**: 212.

Barnes-Velez JA, Aksoy Yasar FB, Hu J. 2023. Myelin lipid metabolism and its role in myelination and myelin maintenance. *Innovation (Camb)* **4**: 100360.

Berg MD, Brandl CJ. 2021. Transfer RNAs: diversity in form and function. *RNA Biol* **18**: 316-339.

Bernard G, Chouery E, Putorti ML, Tetreault M, Takanohashi A, Carosso G, Clement I, Boespflug-Tanguy O, Rodriguez D, Delague V et al. 2011. Mutations of POLR3A encoding a catalytic subunit of RNA polymerase Pol III cause a recessive hypomyelinating leukodystrophy. *Am J Hum Genet* **89**: 415-423.

Bonhoure N, Byrnes A, Moir RD, Hodroj W, Preitner F, Praz V, Marcelin G, Chua SC, Jr., Martinez-Lopez N, Singh R et al. 2015. Loss of the RNA polymerase III repressor MAF1 confers obesity resistance. *Genes Dev* **29**: 934-947.

Brodkin J, Frank D, Grippo R, Hausfater M, Gulinello M, Achterholt N, Gutzen C. 2014. Validation and implementation of a novel high-throughput behavioral phenotyping instrument for mice. *J Neurosci Methods* **224**: 48-57.

Butovsky O, Weiner HL. 2018. Microglial signatures and their role in health and disease. *Nat Rev Neurosci* **19**: 622-635.

Choquet K, Forget D, Meloche E, Dicaire MJ, Bernard G, Vanderver A, Schiffmann R, Fabian MR, Teichmann M, Coulombe B et al. 2019. Leukodystrophy-associated POLR3A mutations down-regulate the RNA polymerase III transcript and important regulatory RNA BC200. *J Biol Chem* **294**: 7445-7459.

Costa-Mattioli M, Walter P. 2020. The integrated stress response: From mechanism to disease. *Science* **368**: eaat5314.

Dergai O, Cousin P, Gouge J, Satia K, Praz V, Kuhlman T, Lhote P, Vannini A, Hernandez N. 2018. Mechanism of selective recruitment of RNA polymerases II and III to snRNA gene promoters. *Genes Dev* **32**: 711-722.

Dorboz I, Dumay-Odelot H, Boussaid K, Bouyacoub Y, Barreau P, Samaan S, Jmel H, Eymard-Pierre E, Cances C, Bar C et al. 2018. Mutation in POLR3K causes hypomyelinating leukodystrophy and abnormal ribosomal RNA regulation. *Neurol Genet* **4**: e289.

Gao W, Gallardo-Dodd CJ, Kutter C. 2022. Cell type-specific analysis by single-cell profiling identifies a stable mammalian tRNA-mRNA interface and increased translation efficiency in neurons. *Genome Res* **32**: 97-110.

Gao Z, Herrera-Carrillo E, Berkhout B. 2018. RNA Polymerase II Activity of Type 3 Pol III Promoters. *Mol Ther Nucleic Acids* **12**: 135-145.

Hammelrath L, Skokic S, Khmelinskii A, Hess A, van der Knaap N, Staring M, Lelieveldt BPF, Wiedermann D, Hoehn M. 2016. Morphological maturation of the mouse brain: An in vivo MRI and histology investigation. *Neuroimage* **125**: 144-152.

Hayashi S, McMahon AP. 2002. Efficient recombination in diverse tissues by a tamoxifen-inducible form of Cre: a tool for temporally regulated gene activation/inactivation in the mouse. *Dev Biol* **244**: 305-318.

Hillary RF, FitzGerald U. 2018. A lifetime of stress: ATF6 in development and homeostasis. *J Biomed Sci* **25**: 48.

Hughes LA, Rudler DL, Siira SJ, McCubbin T, Raven SA, Browne JM, Ermer JA, Rientjes J, Rodger J, Marcellin E et al. 2023. Copy number variation in tRNA isodecoder genes impairs mammalian development and balanced translation. *Nat Commun* **14**: 2210.

Ishimura R, Nagy G, Dotu I, Chuang JH, Ackerman SL. 2016. Activation of GCN2 kinase by ribosome stalling links translation elongation with translation initiation. *Elife* **5**: e14295.

Ishimura R, Nagy G, Dotu I, Zhou H, Yang XL, Schimmel P, Senju S, Nishimura Y, Chuang JH, Ackerman SL. 2014. RNA function. Ribosome stalling induced by mutation of a CNS-specific tRNA causes neurodegeneration. *Science* **345**: 455-459.

James Faresse N, Canella D, Praz V, Michaud J, Romascano D, Hernandez N. 2012. Genomic study of RNA polymerase II and III SNAPc-bound promoters reveals a gene transcribed by both enzymes and a broad use of common activators. *PLoS Genet* **8**: e1003028.

Kapur M, Ganguly A, Nagy G, Adamson SI, Chuang JH, Frankel WN, Ackerman SL. 2020. Expression of the Neuronal tRNA n-Tr20 Regulates Synaptic Transmission and Seizure Susceptibility. *Neuron* **108**: 193-208 e199.

Kleeff J, Whitcomb DC, Shimosegawa T, Esposito I, Lerch MM, Gress T, Mayerle J, Drewes AM, Rebours V, Akisik F et al. 2017. Chronic pancreatitis. *Nat Rev Dis Primers* **3**: 17060.

Lata E, Choquet K, Sagliocco F, Brais B, Bernard G, Teichmann M. 2021. RNA Polymerase III Subunit Mutations in Genetic Diseases. *Front Mol Biosci* **8**: 696438.

Leto K, Arancillo M, Becker EB, Buffo A, Chiang C, Ding B, Dobyns WB, Dusart I, Haldipur P, Hatten ME et al. 2016. Consensus Paper: Cerebellar Development. *Cerebellum* **15**: 789-828.

Li D, Zhang J, Liu Q. 2022. Brain cell type-specific cholesterol metabolism and implications for learning and memory. *Trends Neurosci* **45**: 401-414.

Love MI, Huber W, Anders S. 2014. Moderated estimation of fold change and dispersion for RNA-seq data with DESeq2. *Genome Biol* **15**: 550.

McKenzie AT, Wang M, Hauberg ME, Fullard JF, Kozlenkov A, Keenan A, Hurd YL, Dracheva S, Casaccia P, Roussos P et al. 2018. Brain Cell Type Specific Gene Expression and Co-expression Network Architectures. *Sci Rep* **8**: 8868.

Merheb E, Cui MH, DuBois JC, Branch CA, Gulinello M, Shafit-Zagardo B, Moir RD, Willis IM. 2021. Defective myelination in an RNA polymerase III mutant leukodystrophic mouse. *Proc Natl Acad Sci U S A* **118(40)**: e2024378118.

Nishiyama A, Shimizu T, Sherafat A, Richardson WD. 2021. Life-long oligodendrocyte development and plasticity. *Semin Cell Dev Biol* **116**: 25-37.

Nwagwu M, Nana M. 1980. Ribonucleic acid synthesis in embryonic chick muscle, rates of synthesis and half-lives of transfer and ribosomal RNA species. *J Embryol Exp Morphol* **56**: 253-267.

Park J, Park J, Lee J, Lim C. 2021. The trinity of ribosome-associated quality control and stress signaling for proteostasis and neuronal physiology. *BMB Rep* **54**: 439-450.

Perrier S, Gauquelin L, Fallet-Bianco C, Dishop MK, Michell-Robinson MA, Tran LT, Guerrero K, Darbelli L, Srour M, Petrecca K et al. 2020. Expanding the phenotypic and molecular spectrum of RNA polymerase III-related leukodystrophy. *Neurol Genet* **6**: e425.

Perrier S, Gauquelin L, Wambach JA, Bernard G. 2022. Distinguishing severe phenotypes associated with pathogenic variants in POLR3A. *Am J Med Genet A* **188**: 708-712.

Pinkard O, McFarland S, Sweet T, Coller J. 2020. Quantitative tRNA-sequencing uncovers metazoan tissue-specific tRNA regulation. *Nat Commun* **11**: 4104.

Quiros PM, Goyal A, Jha P, Auwerx J. 2017. Analysis of mtDNA/nDNA Ratio in Mice. *Curr Protoc Mouse Biol* **7**: 47-54.

Saher G, Stumpf SK. 2015. Cholesterol in myelin biogenesis and hypomyelinating disorders. *Biochim Biophys Acta* **1851**: 1083-1094.

Spaulding EL, Hines TJ, Bais P, Tadenev ALD, Schneider R, Jewett D, Pattavina B, Pratt SL, Morelli KH, Stum MG et al. 2021. The integrated stress response contributes to tRNA synthetase-associated peripheral neuropathy. *Science* **373**: 1156-1161.

Taylor SC, Nadeau K, Abbasi M, Lachance C, Nguyen M, Fenrich J. 2019. The Ultimate qPCR Experiment: Producing Publication Quality, Reproducible Data the First Time. *Trends Biotechnol* **37**: 761-774.

Tepper JM, Bolam JP. 2004. Functional diversity and specificity of neostriatal interneurons. *Curr Opin Neurobiol* **14**: 685-692.

Terrey M, Adamson SI, Gibson AL, Deng T, Ishimura R, Chuang JH, Ackerman SL. 2020. GTPBP1 resolves paused ribosomes to maintain neuronal homeostasis. *Elife* **9**: e62731.

Torrence ME, MacArthur MR, Hosios AM, Valvezan AJ, Asara JM, Mitchell JR, Manning BD. 2021. The mTORC1-mediated activation of ATF4 promotes protein and glutathione synthesis downstream of growth signals. *Elife* **10**: e63326.

Watt KE, Macintosh J, Bernard G, Trainor PA. 2023. RNA Polymerases I and III in development and disease. *Semin Cell Dev Biol* **136**: 49-63.

Wolf NI, Vanderver A, van Spaendonk RM, Schiffmann R, Brais B, Bugiani M, Sistermans E, Catsman-Berrevoets C, Kros JM, Pinto PS et al. 2014. Clinical spectrum of 4H leukodystrophy caused by POLR3A and POLR3B mutations. *Neurology* **83**: 1898-1905.

Yee NS, Gong W, Huang Y, Lorent K, Dolan AC, Maraia RJ, Pack M. 2007. Mutation of RNA Pol III subunit rpc2/polr3b Leads to Deficiency of Subunit Rpc11 and disrupts zebrafish digestive development. *PLoS Biol* **5**: e312.

Zeiss CJ. 2021. Comparative Milestones in Rodent and Human Postnatal Central Nervous System Development. *Toxicol Pathol* **49**: 1368-1373.

Zuko A, Mallik M, Thompson R, Spaulding EL, Wienand AR, Been M, Tadenev ALD, van Bakel N, Sijlmans C, Santos LA et al. 2021. tRNA overexpression rescues peripheral neuropathy caused by mutations in tRNA synthetase. *Science* **373**: 1161-1166.

Figures

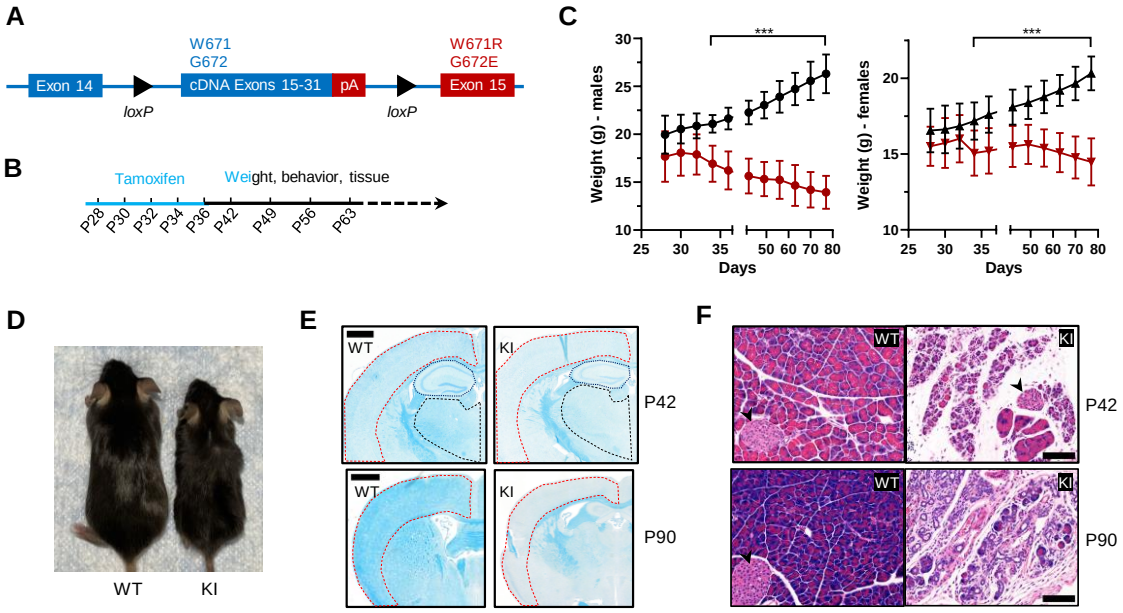

Figure 1. Body weight, length and histological characteristics of Polr3a-tamKI mice.
(***A***) Schematic of the modified *Polr3a* locus showing floxed WT sequences encoding exons 15-31 with adjacent sequences for termination and polyadenylation (pA) and *Polr3a* exon15 containing the leukodystrophy mutations.
(***B***) Tamoxifen injections and experimental timeline.
(***C***) Lower body weights of Polr3a-tamKI (red) versus WT (black) mice (males n=18/group, nested t test p<0.0001****, females n= 20/group, nested t test p<0.0001****). Data show mean ± SD.
(***D***) Body length differences at P56. Images are representative.
(***E***) LFB-staining of WT and KI brain sections at P42 and P90. The cerebral cortex, hippocampus and thalamus are marked by red, blue and black lines, respectively. Scale bar, 1000 µm.
(***F***) H&E-stained WT and KI pancreata at P42 and P90 shows a dramatic loss of acinar cells. Pancreatic islets are marked with a black arrowhead. Scale bar,100 µm.

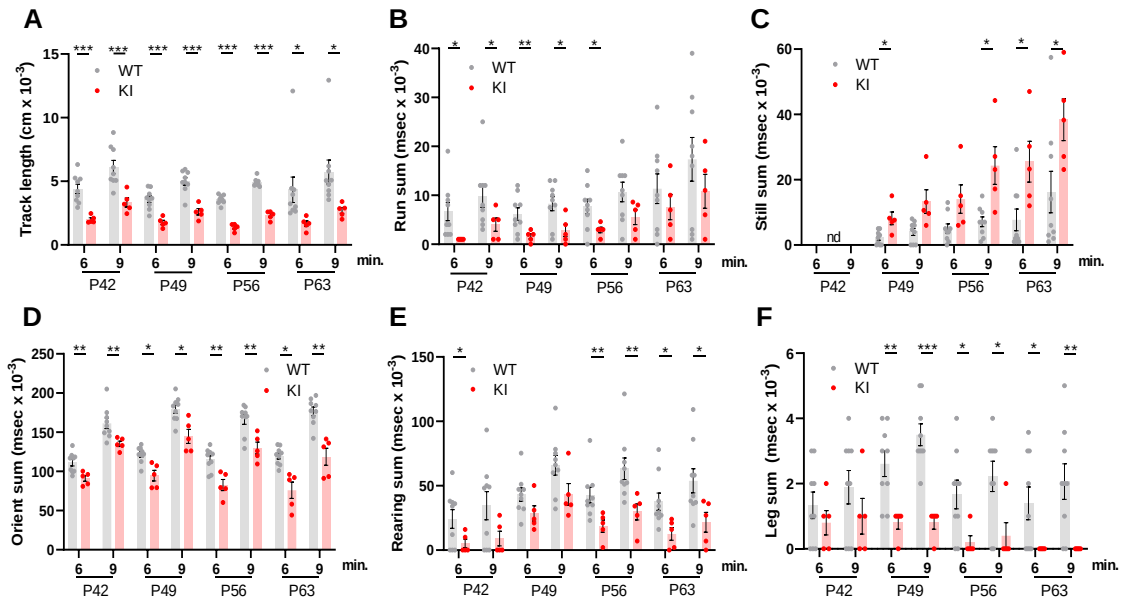

Figure 2. Behavioral studies of WT and Polr3a-tamKI mice.
(***A-C***) Locomotor activity is reported as the total distance traveled (Track length) and the total time during which the mice are running (Run sum) or standing still (Still sum).
(***D***) Risk assessment (Orient sum) is the sum of three orientation behaviors (see Supplemental Fig. S3).
(***E***) Exploratory behavior (Rear sum) is the sum of three rearing behaviors (see Supplemental Fig. S3).
(***F***) Leg grooming. Data were collected at weekly intervals beginning at P42 (WT n= 9 and KI n= 5). Mice were tested for nine minutes with recording in three intervals of three minutes each. Values show the mean ± SEM at six- and nine-minute timepoints. Multiple t tests and one-way ANOVA, * $p<0.05$, ** $p < 0.01$, *** $p < 0.001$.

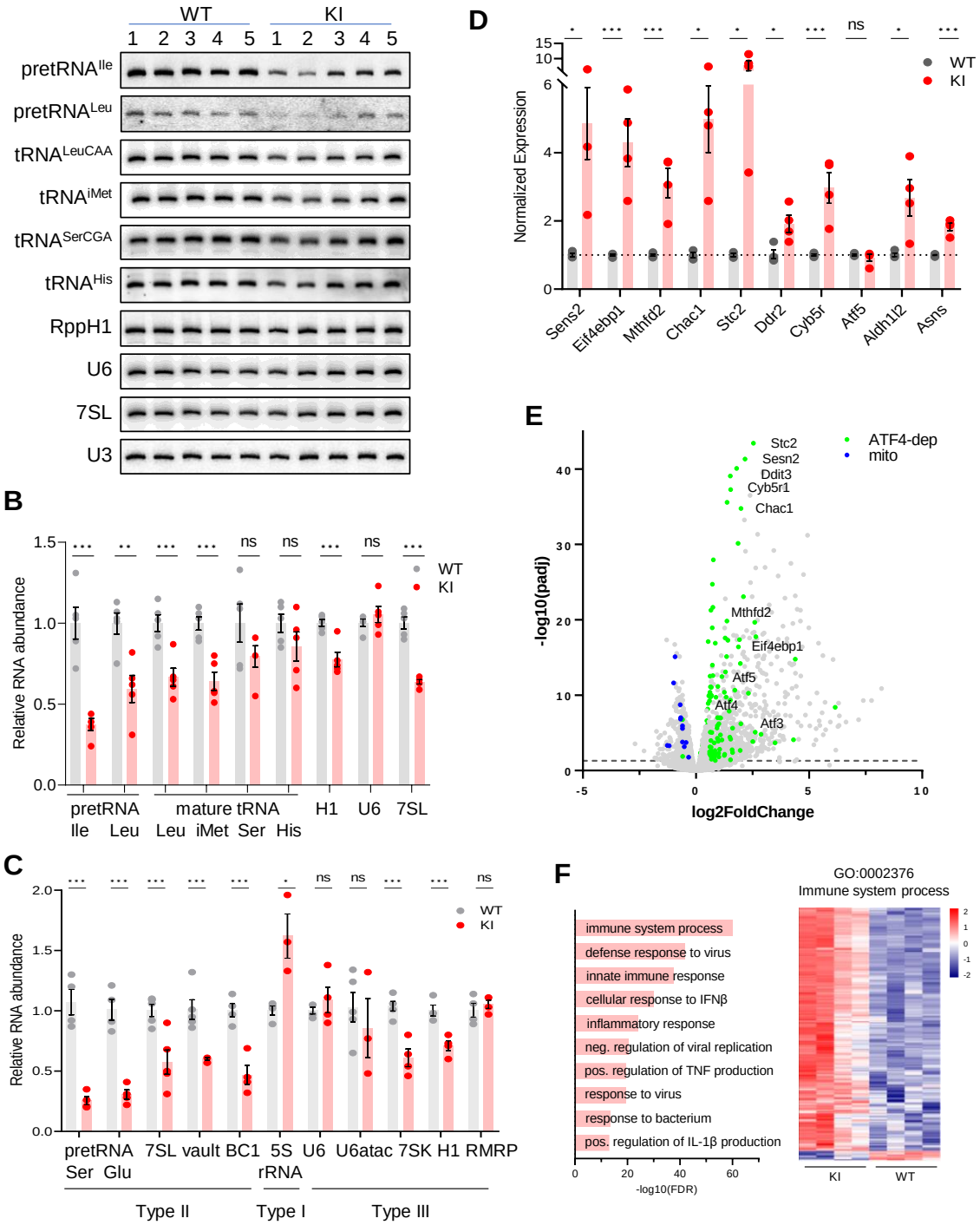
WT
KI
1 2 3 4 5 1 2 3 4 5
pretRNA^Ile
pretRNA^Leu
tRNA^LeuCAA
tRNA^iMet
tRNA^SerCGA
tRNA^His
RppH1
U6
7SL
U3
B
Relative RNA abundance
WT
KI
pretRNA
Ile Leu
mature tRNA
Leu iMet Ser His
H1
U6
7SL
C
Relative RNA abundance
WT
KI
pretRNA
Ser Glu
7SL
vault
BC1
5S
rRNA
U6
U6atac
7SK
H1
RMRP
Type II
Type I
Type III
D
Normalized Expression
WT
KI
Sens2
Eif4ebp1
Mthfd2
Chac1
Stc2
Ddr2
Cyb5r
Atf5
Aldh1l2
Asns
E
ATF4-dep
mito
Stc2
Sesn2
Ddit3
Cyb5r1
Chac1
Mthfd2
Eif4ebp1
Atf5
Atf4
Atf3
-log10(padj)
log2FoldChange
F
GO:0002376
Immune system process
immune system process
defense response to virus
innate immune response
cellular response to IFNβ
inflammatory response
neg. regulation of viral replication
pos. regulation of TNF production
response to virus
response to bacterium
pos. regulation of IL-1β production
-log10(FDR)
KI
WT

Figure 3. Transcriptome analysis of Polr3a-tamKI cerebra at P75.
(***A***) Northern blot of Pol III transcripts. Precursor tRNAs (Ile-TAT, Leu-CAA), mature tRNAs (Leu-CAA, iMet, Ser-CGA, His), RppH1, U6 and 7SL RNAs and the loading control U3 snRNA were detected by hybridization using transcript-specific oligonucleotide probes. All blots represent sequential probing of a single gel. The cropped images frame the relevant regions.
(***B***) Quantitation of Pol III transcripts in panel *A* (mean ± SEM, n= 5 biological replicates).
(***C***) RT-qPCR of Pol III transcript abundance (mean ± SEM, n= 3-6 biological replicates).
(***D***) RT-qPCR of selected ATF4-regulated ISR genes (mean ± SEM, n= 3-5 biological replicates).
(***E***) Global gene expression quantified by RNA-seq. The volcano plot shows gene expression changes (KI/WT, n= 4 biological replicates). Differentially expressed (DE) ATF4-regulated genes (green) (p-adj <0.05, log2FC >|0.58|) and mitochondrially-encoded transcripts (blue). ATF4-regulated genes assayed in panel *D* and Ddit3/Chop are labeled.
(***F***) Top ten GO bioprocesses among up-regulated DE genes are shown with a heatmap of Z-scores for DE genes annotated to the GO:0002376 immune system process. For all graphs: WT, gray bars and circles; KI, red bars and circles. ns, not significant; * p ≤0.05; ** p ≤0.01; *** p ≤0.005.

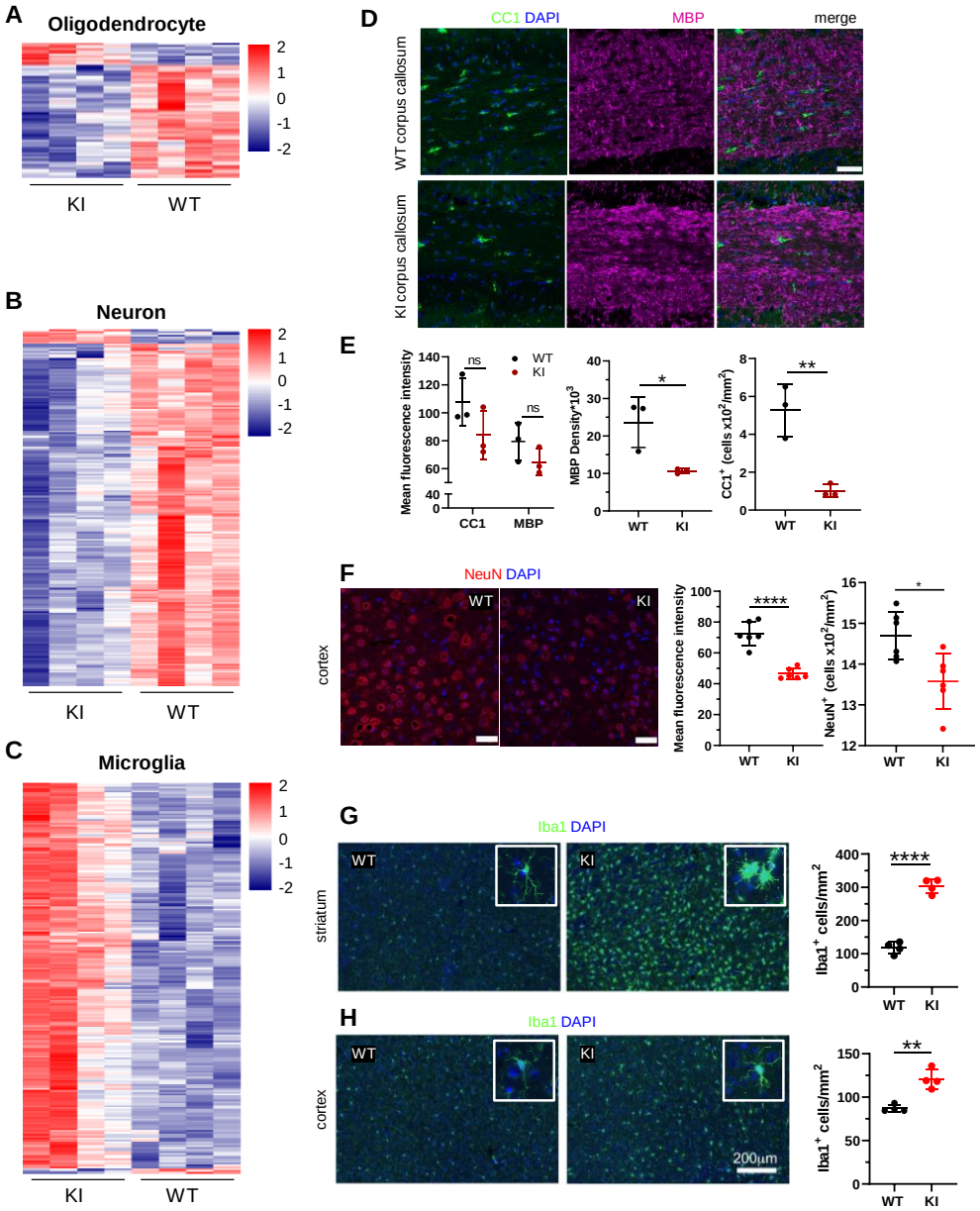
A
Oligodendrocyte
2
1
0
-1
-2
KI
WT
B
Neuron
KI
WT
C
Microglia
KI
WT
D
CC1 DAPI
MBP
merge
WT corpus callosum
KI corpus callosum
E
Mean fluorescence intensity
ns
WT
KI
CC1
MBP
MBP Density*10^3
*
CC1+ (cells x10^2/mm^2)
**
F
NeuN DAPI
cortex
WT
KI
Mean fluorescence intensity
****
NeuN+ (cells x10^2/mm^2)
*
G
Iba1 DAPI
striatum
Iba1+ cells/mm^2
****
H
Iba1 DAPI
cortex
200µm
Iba1+ cells/mm^2
**

Figure 4. Cell type-specific changes in Polr3a-tamKI cerebra at P75.
(***A-C***) Oligodendrocyte (***A***), neuron (***B***), and microglia (***C***) cell type-specific DE genes. Heatmaps show Z-scores of DE genes identified in the top 500 mouse cell type-specific genes defined in McKenzie et al. 2018.
(***D-E***) Immunostaining of oligodendrocytes at the midline of the corpus callosum. Scale bar, 40 µm. Mean fluorescence intensities of MBP and CC1, MBP staining density and CC1 cell counts represent mean ± SD, n= 3.
(***F***) NeuN immunostaining of neurons in the motor cortex. Scale bar, 40 µm. Mean fluorescence intensities and cell counts represent mean ± SD of bilaterally symmetric regions (n= 3).
(***G-H***) Iba1 staining of microglia in the striatum (***G***) and cerebral cortex (***H***). Insets show larger magnifications of individual microglia. Note the striking shortening of processes and enlargement of the cell body in the striatum. Scale bar, 200 µm. Cell counts represent mean ± SD of bilaterally symmetric regions, (n= 2). For all graphs: WT, black; KI, red; ns, not significant; * $p \leq 0.05$; ** $p \leq 0.01$; *** $p \leq 0.005$; **** $p < 0.0001$.

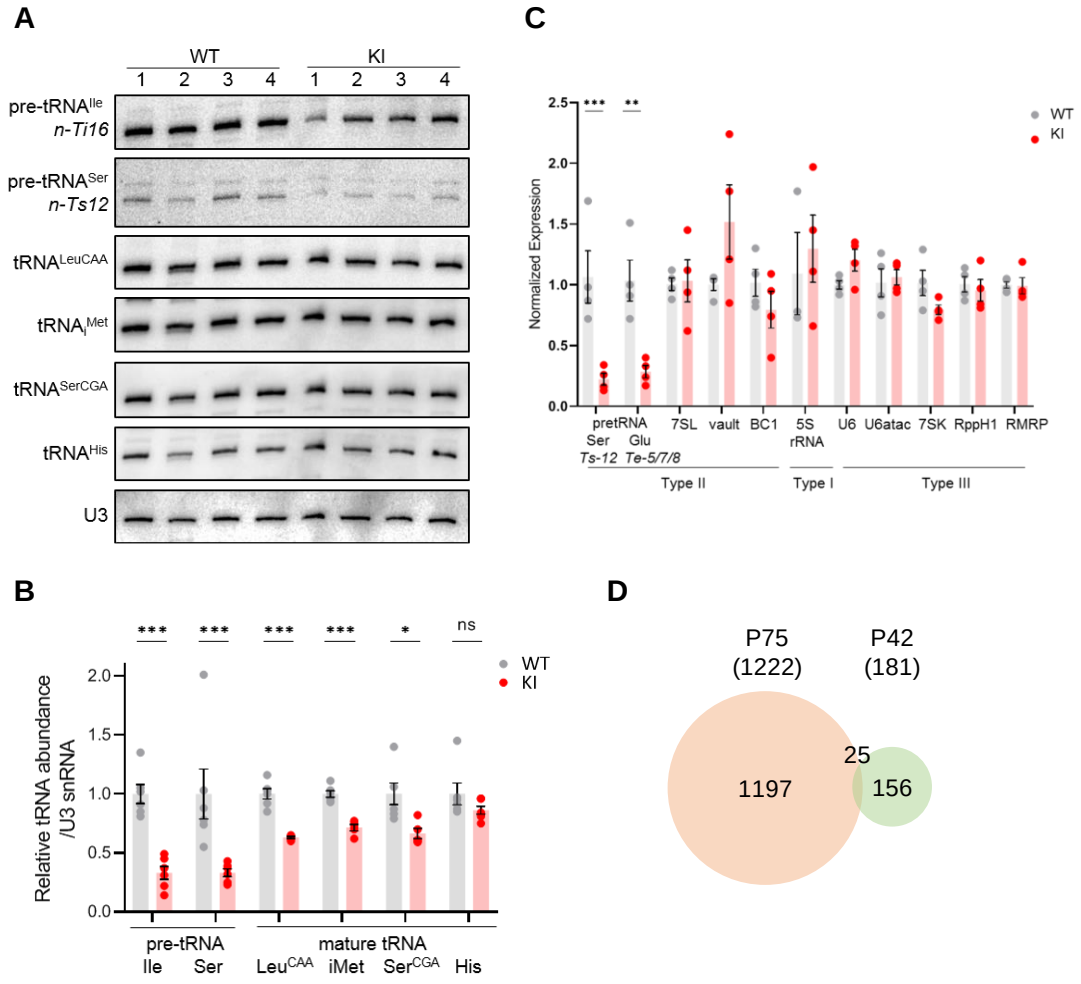

Figure 5. Transcriptome Analysis of Polr3a-tamKI cerebra at P42.
(***A***) Northern blots of Pol III transcripts. Precursor tRNAs (Ile-TAT, Ser-CGA), mature tRNAs (Leu-CAA, iMet, Ser-CGA, His) and U3 snRNA were detected as in Fig. 3A.
(***B***) Quantitation of Pol III transcripts in panel *A*. Mean ± SEM, n= 5 biological replicates.
(***C***) RT-qPCR of Pol III transcript abundance. Mean ± SEM, n= 3-5 biological replicates.
(***D***) Venn diagram of the overlap between P75 and P42 DE genes (p-adj <0.05, log2FC >|0.58|).

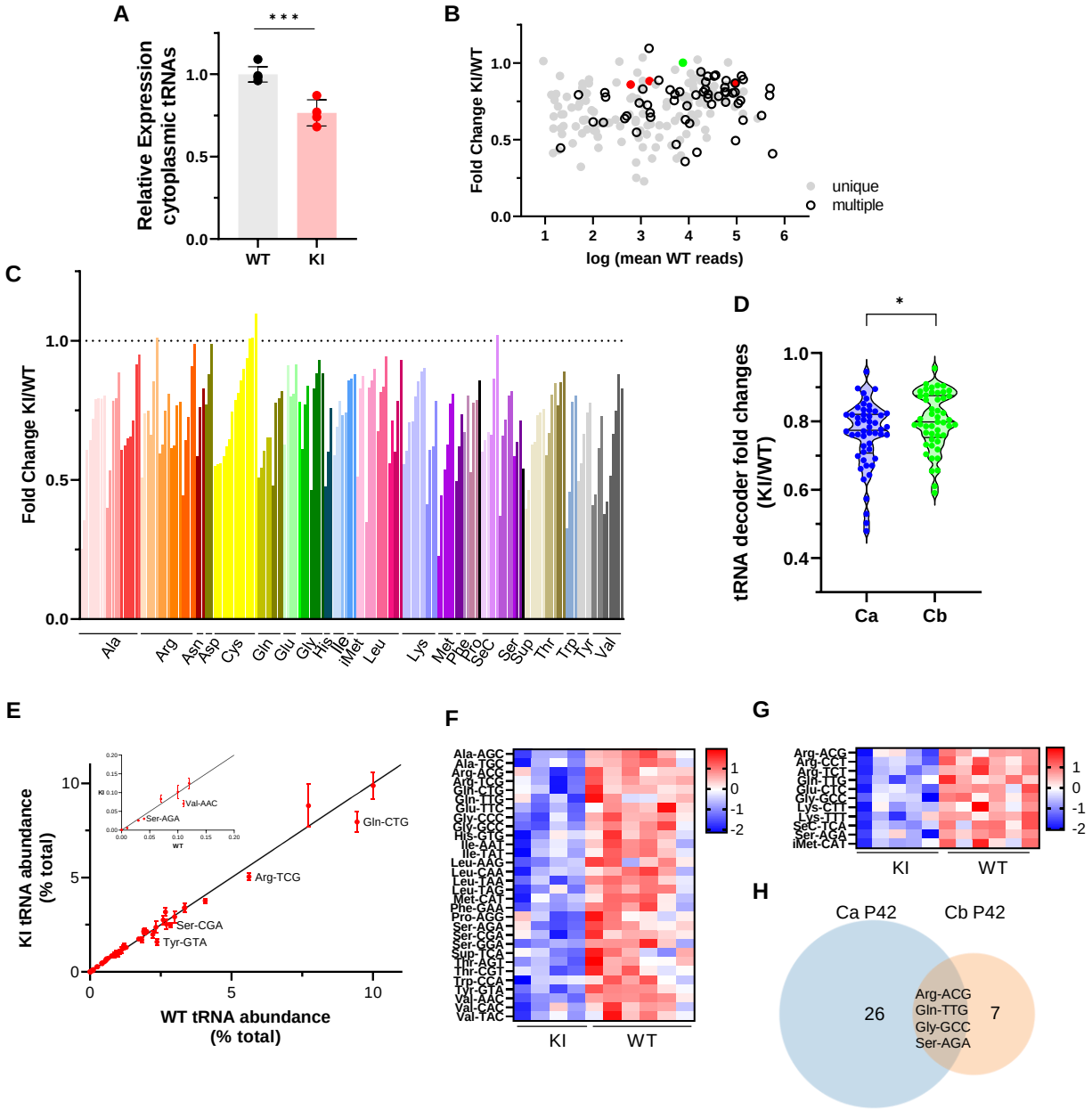
A
Relative Expression cytoplasmic tRNAs
WT
KI
B
Fold Change KI/WT
log (mean WT reads)
unique
multiple
C
Fold Change KI/WT
Ala
Arg
Asn
Asp
Cys
Gln
Glu
Gly
His
Ile
iMet
Leu
Lys
Met
Phe
Pro
SeC
Ser
Sup
Thr
Trp
Tyr
Val
D
tRNA decoder fold changes (KI/WT)
Ca
Cb
E
KI tRNA abundance (% total)
WT tRNA abundance (% total)
Gln-CTG
Arg-TCG
Ser-CGA
Tyr-GTA
Val-AAC
Ser-AGA
F
KI
WT
G
KI
WT
H
Ca P42
Cb P42
26
7
Arg-ACG
Gln-TTG
Gly-GCC
Ser-AGA

Figure 6. Cytosolic tRNA abundance in Polr3a-tamKI cerebra at P42.
(***A***) Total cytoplasmic tRNA reads in WT and KI cerebra, normalized to the sum of spike-in and mitochondrially-encoded tRNA reads are expressed relative to the mean WT value. Mean ± SD, KI n= 4, WT n= 6 biological replicates, p = 0.0003.
(***B***) tRNA fold change (KI/WT) is plotted against Log mean WT reads. Symbols show tRNAs encoded by unique loci (gray), identical tRNAs encoded by multiple loci (hollow black), iMet tRNAs (red) and tRNAArg-TCT-4-1 (green).
(***C***) tRNA fold change (KI/WT) for all decoder families. Individual tRNAs are ordered from most to least fold change and grouped by codon recognition (tRNA decoder family). The amino acid for each tRNA decoder family is indicated.
(***D***) Violin plots of tRNA decoder fold changes (KI/WT) for cerebra (Ca) and cerebella (Cb) at P42. tRNA reads were summed for each tRNA decoder family and normalized to spike-in and mitochondrial tRNA reads, p = 0.0250. For Ca, n= 4 (KI) and n= 6 (WT) biological replicates and for Cb, n= 5 (KI) and n= 6 (WT) biological replicates.
(***E***) The cytoplasmic tRNA profile for KI cerebra is plotted against the WT profile. tRNA decoder reads are expressed as a percentage of their respective total cytoplasmic decoder pool, mean ± SEM. tRNA decoders that are significantly lower in the KI compared to WT ($p \leq 0.05$) fall below the regression line and are labeled. The inset shows tRNA decoders representing <0.2% of the total tRNA pool.
(***F***) DE tRNA decoders in cerebra (Ca).
(***G***) DE tRNA decoders in cerebella (Cb). Heatmaps represent Z scores of normalized read counts for significant DE genes (p-adj <0.05).
(***H***) Venn diagram of the overlap between DE tRNA decoders in Ca and Cb (p-adj <0.05).